

# DESIGN, CONTROL, AND EXPERIMENTAL MODELING OF A MORPHING AIRCRAFT CONFIGURATION

David A. Neal  
 Harry Robertshaw, Advisor  
 Virginia Tech

## Abstract

This work describes the design and construction of a fully adaptive aircraft configuration used as an experimental testbed for aerodynamic modeling and flight control. The adaptive model is designed to achieve large scale shape changes in order to investigate morphing for multi-mission UAVs. There are five independent planform changes along with independent twist control for each wing. Wind tunnel testing was conducted in Virginia Tech's Stability tunnel to analyze the aerodynamic characteristics and evaluate the usefulness of having a UAV with multiple configuration capability. Wind tunnel tests of various planform configurations indicate that different configurations yields minimum drag over a range of flight conditions.

## Introduction

Recent interest in morphing aircraft has motivated the study of variable planform aircraft for low-speed flight<sup>1-5</sup>. Bowman *et. al.*<sup>1</sup> discusses the performance benefits of variable wing area and variable sweep configurations. Separate variable sweep<sup>4</sup> and variable span<sup>5</sup> wind tunnel models have been constructed and tested by others. Relevant discussions of the variable planform capability of birds are presented by Tucker<sup>6</sup> and Tucker and Parrott<sup>7</sup>. They show how a bird varies its wing area to maintain low drag as its gliding speed varies. Kress<sup>8</sup> and Poisson-Quinton<sup>9</sup> discuss the aerodynamics of variable sweep wings, although their focus is on the use of variable sweep for transonic and supersonic flight.

This work has motivated the design and construction of a variable geometry aircraft model for wind tunnel testing. Experimental analysis of a vehicle with both span and sweep variation can be used to support theoretical developments. Significant to variable-geometry aircraft is the issue of flight control, specifically longitudinal stability changes while morphing. An experimental model provides the opportunity to investigate stabilizing aircraft as they transition through different planform configurations.

## Overview of an Adaptive Aircraft Configuration

A major effort of this work is in the design and construction of the adaptive aircraft model. The difficulty comes from the large number of control effectors required for seven independent motions. Each

wing can increase span, vary sweep, and control positive or negative wing twist. In addition to the three independent variations of each wing, the tail can also contract and extend. This results in a 7-DOF experimental model.

The overall vehicle layout and configuration changes are pictured in Figure 1. Each wing can change length between a nominal length of 17 inches and a maximum length of 24.5 inches, a 44% increase. The sweep of each wing can be varied between 0 and 40 degrees, while wing twist can be controlled between  $\pm 20$  degrees. Tail contraction/extension is used as an independent mechanism to control the aerodynamic center location as the wing changes sweep and span. The nominal tail position is extended and can contract 6 inches which causes the overall fuselage chord length to decrease by 12%.

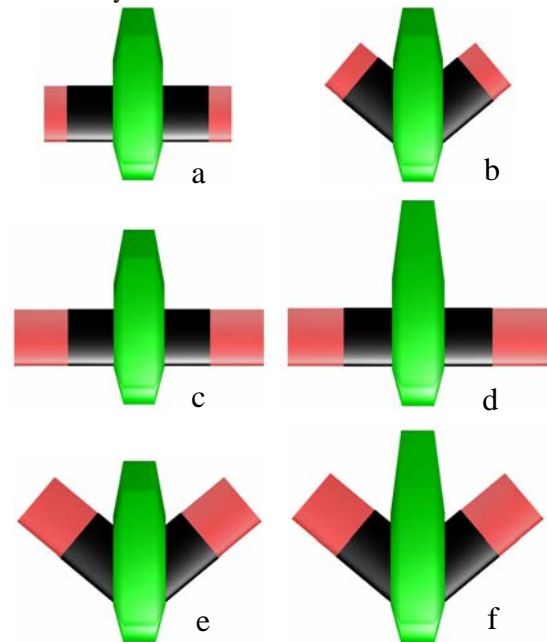


**Figure 1.** Various configurations of the adaptive aircraft model,  
 a)  $\Delta b=0, t=0, A=0$  b)  $\Delta b=0, t=0, A=100\%$  c)  $\Delta b=100\%, t=0, A=0$   
 d)  $\Delta b=100\%, t=100\%, A=0$  e)  $\Delta b=100\%, t=0, A=100\%$   
 f)  $\Delta b=100\%, t=100\%, A=100\%$

The variables  $\Delta b$ ,  $t$ , and  $A$  represent the respective span, tail, and sweep variations as a percentage of their maximum change. The aspect ratio ranges from a minimum of 1.4 to a maximum of 3.24, an increase of 131%. The planform area changes from 935 to 1228 in<sup>2</sup>, a 31% increase.

Precise feedback control allows the model to operate at any point between the maximum and

minimum ranges, permitting an infinite number of configurations for static and dynamic testing. A unique aspect of the vehicle is its ability to achieve anti-symmetric configurations due to the independent control of each wing.

### External Vehicle Design

The wing and fuselage are both designed from modified airfoil sections as seen in Figure 2. The wing airfoil sections are modified NACA 0020-64's, and have a 14-inch chord. The modification shifts the maximum thickness closer to the center of the airfoil section to create space for internal actuators. The fuselage design is an interpolation between two different airfoil sections. The mid-section of the fuselage is an extruded NACA 0017-64 with a chord length of 49 inches. On each end, the extruded section tapers down to a NACA 0020-65 with a 21 inch chord. This shape creates enough space for the wings to sweep in without contacting the fuselage. Designing the fuselage as an airfoil streamlines the design, increasing the overall vehicle lift while decreasing drag.

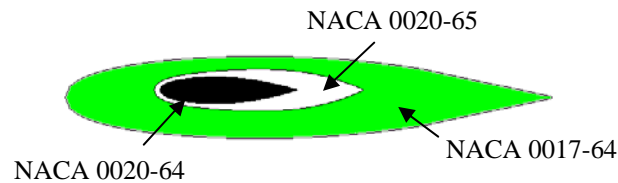


**Figure 2.** Vehicle cross-section detailing individual airfoil sections

### Internal Vehicle Design Overview

The model uses two rotational actuators and five linear actuators to control the wing shape. The sweep actuators are electromechanical while all other actuators are pneumatic. Pneumatic actuators were chosen for the wing and tail extensions because for large strokes, they are lighter than hydraulic or electromechanical actuators. To control wing twist, it was necessary to have a small actuator that generated enough torque to deform a semi-rigid wing section, while still being relatively light. A small rotary pneumatic actuator was chosen to drive the twist mechanism because it could produce the high torque required at a low overall weight. The sweep design requires that the actuator directly support the aerodynamic forces against the wing. A lead screw electromechanical actuator was chosen because it is nonbackdrivable under load. The internal model and actuators are shown in Figure 3. The different subsystems include the span extension, the twist mechanism, the sweep system, tail actuation, and the control circuit.

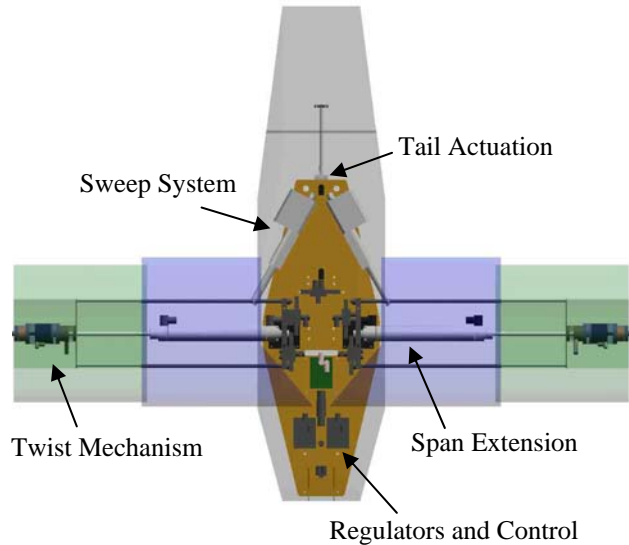


**Figure 3.** Overview of internal vehicle structure

### Span Actuation

Off-the-shelf pneumatic actuators were used to extend and contract the wing. The cylinder body is a thin-walled stainless steel while the rod is a hard, chrome-plated, carbon steel. The actuators compose the main segment of the wing spar. They have an 8 inch stroke and a 1.5 inch bore. Each actuator has an internal potentiometer for position feedback and is double-acting. There is an individual pressure port to control motion in either direction. A single 3-position solenoid valve directs the flow to each port for both extension and contraction. The valve response time is less than 20 ms, fast enough that a PWM signal is capable of controlling the average pressure input to the cylinder. This removes the need for proportional pressure regulators or proportional solenoid valves. For large-bore cylinders, proportional pressure systems that supply the appropriate flowrate are large and heavy. The cylinder position and rate can both be controlled using a PWM signal to the solenoid valve as the control input. The compensator output in the feedback loop adjusts the duty cycle of the signal to the solenoid valve. For static testing, only steady-state error was a concern, so the goal was a simple control design that could achieve the desired positions. A straightforward proportional-derivative controller was designed because it did not require a system model and the gains could be tuned experimentally. Derivative control was included to increase the effective system damping and provide a smoother actuator response. The span extension can be controlled at a maximum rate of 8 inches per second with a steady-state error of  $\pm 0.05$  inches.

### Twist Actuation

Figure 4 shows the internal mechanism used to control wing twist. It consists of a 2 inch OD pneumatic rotary actuator driving a gear train to produce the required output torque. A rotary potentiometer indicates the absolute rotation of the actuator for feedback. The vane style actuator is double-acting, permitting rotation in either direction up to 270 degrees. At a line pressure of 70 psi, the actuator generates approximately 16 in-lbs of torque. To increase the output torque, the actuator drives a single-stage planetary gear train with a reduction of 6.67. The total system output is 106.6 in-lbs of torque and 40.54 degrees of rotation ( $\approx \pm 20$  degrees) at 70 psi. The output linkage of the planetary set guides a keyed shaft that passes through a bearing and rotates a keyed airfoil section. The acrylic airfoil is bonded to a flexible, closed-cell polyethylene wing section with a fixed boundary condition at the root. This causes a linear twist distribution to result when the internal twist mechanism rotates as shown in Figure 5. The flexible wing slides inside a hollow, rigid, fiberglass wing which enforces the fixed boundary condition for rotation. To permit independent twist and span motions, the twist mechanism is attached to the end of the span cylinder rod. While this decouples the two motions, the wing area that is twisting changes with span so that the motions are still coupled aerodynamically. That is, the twist control authority increases with span due to increases in both effective wing area and the moment arm.

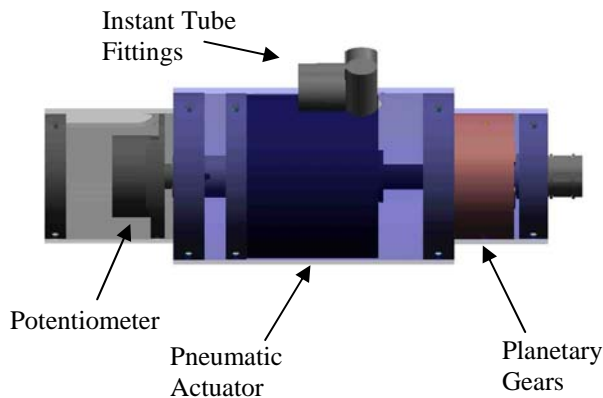


**Figure 4.** Internal view of twist mechanism

The wing twist must be controlled within very small increments because minor changes generate significant aerodynamic forces. To achieve such precise control, an electro-pneumatic pressure regulator was used to adjust the input pressure to the cylinder. The pressure regulator is a closed-loop system that contains a servo-valve that fires at the appropriate rate to control the average output pressure. The output of the pressure

regulator passes through a 3-position solenoid valve depending on the direction of rotation.

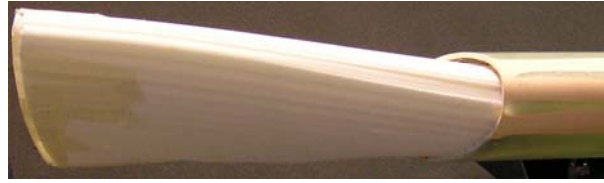


**Figure 5.** Linear twist distribution due to internal actuation

### Sweep Actuation

The wing sweep is controlled by two electromechanical, lead-screw actuators. The actuators are non-backdrivable, and can generate 25-lbs of force, sufficient for controlling sweep while under aerodynamic loading. The sweeping motion is actually the output of a 3-bar linkage where the actuator forms one of the links that directly drives the system. The layout is shown in Figure 6. While the design is simple, the model to correlate actuator motion to sweep angle is governed by coupled, transcendental equations describing the linkage motion as a function of the actuator length change.

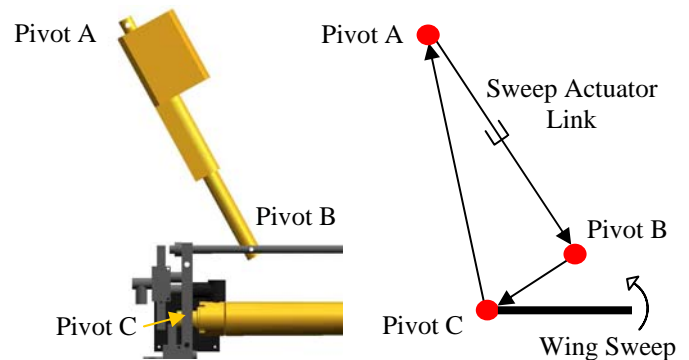


**Figure 6.** Direct-drive sweep geometry

The only feedback for the direct-drive system is the sweep angle from potentiometers attached to the pivot rotation of the wings, Pivot C in Figure 6. While this provides a direct measurement of the absolute sweep angle, actuator length is another unknown in the equations of motion. Rather than include additional sensors, the actuator length is approximated from the sweep angle and the equations governing the 3-bar linkage.

The actuators operate at 24V and draw 2.5A each, at maximum load. Similar to the span actuation, to achieve a proportional type of control signal a pulse-width-modulated voltage signal was sent to the actuator to regulate the average current applied. The initial control model (for static wind-tunnel testing) consisted of a simple feedback loop with a proportional-derivative controller and a deadband to prevent

oscillations around the desired position. The controlled maximum sweep rate is 30 degrees per second with  $\pm 0.3$  degrees steady-state error.

### Wing Assembly

The effective wing spar is composed of the span cylinder with the attached twist mechanism. At the root, a lexan bar holds the span actuator, and two small steel rods that extend with the wing. Acrylic airfoil sections connect the two rods and the cylinder to form a solid member. This 3-bar segment provides a constraining torque for the twist mechanism to prevent rotation of the span cylinder rod when twisting the outer wing. This connection is mounted to a ball-bearing turntable to create a low friction rotation surface for sweep. Figure 7 illustrates the entire wing assembly.

The sweep actuator connects directly to the rear constraining rod so that the entire wing mechanism rotates as the linear actuator contracts. Two pivot rods extend from the turntables and are connected by a small, steel turnbuckle that takes compressive loads as the lift force attempts to raise the wings and tensile loads to support the weight of the wings when unloaded. The turnbuckle effectively carries whatever load necessary to maintain a level wing orientation whether loaded or unloaded. This also keeps the turntables level so that a low-friction sweep surface is maintained.

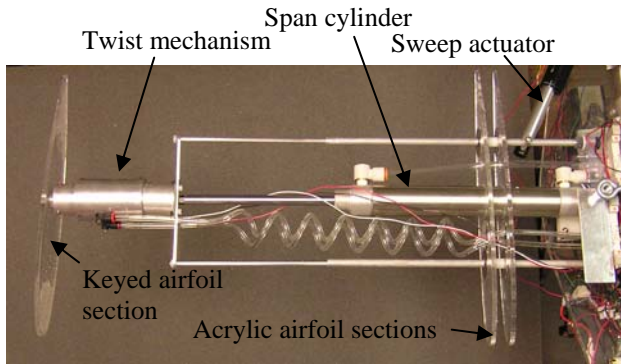


Figure 7. Extended wing section showing 3-bar segment

### Tail Actuation

The tail extension uses the same style of actuator as the span, with a built-in feedback circuit. The differences are that the tail actuator is 6-inches long and only has a 1-1/16 inch bore. To achieve precise control, the same electro-pneumatic pressure regulator was used as with the twist. The regulator outputs to a 3-position solenoid valve to control the double-acting cylinder. Accurate position control was achieved using only proportional control.

### Control Circuit

Onboard control and data acquisition is accomplished using PC/104 boards with special software for implementing control systems designed in the Matlab/Simulink environment. The PC/104 form-factor consists of individual computer boards, 3.55 x 3.775 inches with 8-bit and 16-bit data buses that can be connected in stacks to create embedded systems. The stack onboard the adaptive model consists of five boards connected to a 16-bit extender that allows side-by-side mounting. The stack includes a CPU board with a 233-Mhz processor, a 12-bit 100kHz D/A board for controlling the electro-pneumatic pressure regulators, and a 12-bit 500kHz A/D board for measuring potentiometer values. In addition, there is a 16-channel relay board for electronic switching of the solenoid valves and the sweep actuators. The final board is a power supply that regulates the power input to the CPU (e.g., battery).

An overview of the hardware circuit is shown in Figure 8. The CPU processes the Simulink control diagram and controls the additional boards in the PC/104 stack. All potentiometer inputs are measured by the A/D board, while the regulator control signals are output from the D/A board to the twist and tail circuits. The relay board controls all of the solenoid valves for the pneumatic actuators and provides a PWM voltage signal for the sweep actuators.

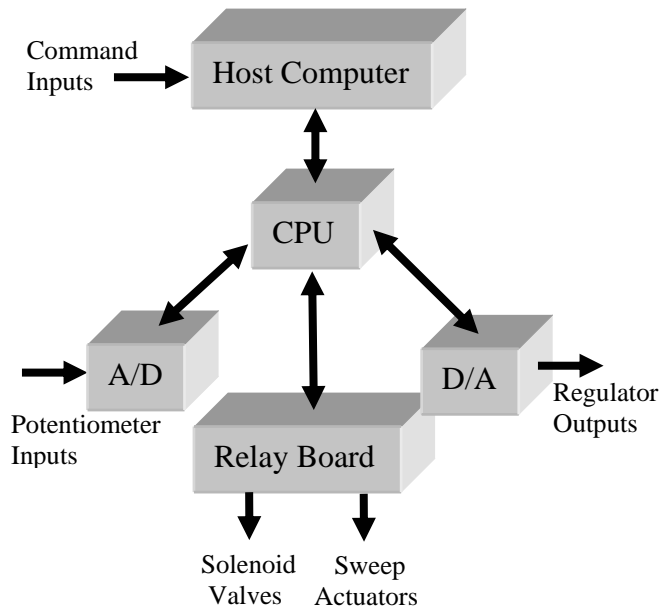


Figure 8. Integration of computer hardware into control circuit

The implementation software directly converts Simulink diagrams to C-code and embeds them into the CPU. There are driver blocks to access and control all of the boards from Simulink which allows realization of both simple and complex control schemes. The

Simulink model is downloaded to the stack and controlled through the CPU board's Ethernet connection. This allows wireless communication if an Ethernet-to-wireless bridge is connected to the Ethernet port on the CPU. When the Simulink model is running on the host computer, any changes made are implemented real-time on the CPU board. For static control, the model consists of multiple feedback control loops for each actuator. The true power of the system comes in later design phases because complex nonlinear control designs can be implemented for autonomous flight control testing.

### Mass Center Motion

The wings comprise a large percentage of the vehicle gross weight due to the internal actuators. Figure 9 illustrates the center-of-gravity (*c.g.*) shift that occurs when the sweep and span are changed. Considering only symmetric sweep and span variations, the *x*-coordinate of the *c.g.* is

$$x_{cg} = \frac{m_b r_b + 2m_w (ar_w + b) \sin \theta_{sw}}{m_b + 2m_w} \quad (1)$$

where  $m_b$  and  $r_b$  are the mass and *c.g.* location of the nonmoving components,  $m_w$  is the wing mass,  $ar_w + b$  represents the *c.g.* shift of the wing due to the span cylinder extension  $r_w$ , and  $\theta_{sw}$  is the wing sweep angle.

Evaluating for the vehicle components, the *c.g.* location shifts from 31.46% of the reference chord (1.81 feet) at zero sweep to 42.47% at full sweep and wing extension, a change of approximately 11%. As will be shown later, the aerodynamic center shifts aft by almost 26% for the same planform changes. Therefore, there is still a net stabilizing effect when the wings sweep, in spite of the *c.g.* shift. By designing the *c.g.* location of the nonmoving components further aft, the tail can be used as an independent agent to alter the stability margin for enhanced maneuvering when the wings are swept.

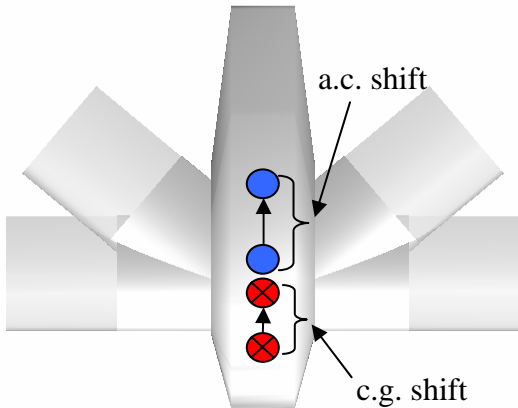


Figure 9. Relative shift in center of gravity and aerodynamic center as wings extend and sweep back

### Effect of a Variable Planform on the Drag

This section presents a brief discussion on the approximate effects of a variable planform on drag. Past research on the gliding of birds by Tucker<sup>6,7</sup> provide relevant discussions on variable span effects for low speed flight. The analysis presented here will follow Tucker's study of variable span effects. The effect of variable sweep and variable tail extension will then be discussed qualitatively based on the results of the variable span analysis.

Consider the unswept planform geometry shown in Figure 10. The planform area can be written as

$$S = S_1 + 2\Delta b c \quad (2)$$

where  $S_1$  is the area when  $\Delta b = 0$  and  $c$  is the chord length of the outer wing section. The reference area ( $S_{ref}$ ) will be defined as  $S_1$ .

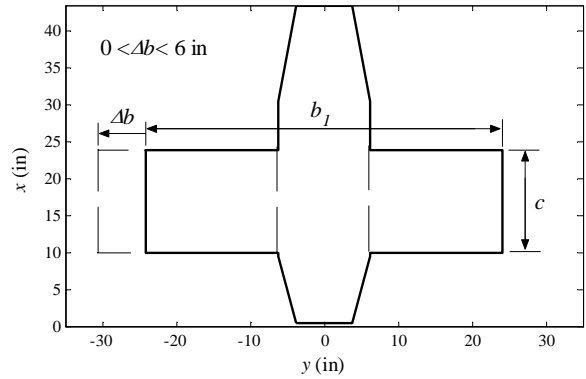


Figure 10. Illustration of the planform parameters for the unswept, tail retracted configuration

For the planform shown in Figure 10, a simplified model for the profile drag can be written as

$$D_p = q S_{ref} C_{dp} \left( 1 + \frac{2\Delta b c}{S_{ref}} \right) \quad (3)$$

where  $q$  is the dynamic pressure and  $C_{dp}$  may be considered a 2-D profile drag coefficient (which is a function of the Reynolds number). A more elaborate profile drag model that uses lift-dependent 2-D drag polars could be used, but for the present analysis, where trends are of interest, Eq. (3) is sufficient. The induced drag for an elliptic load distribution can be written as

$$D_i = \frac{L^2}{\pi q b^2} \quad (4)$$

where  $L$  is the lift force and  $b$  is the total span. A span efficiency factor (as a function of  $\Delta b$ ) could be added to Eq. (4) to account for the effect of a non-elliptic load distribution. This is not included here because the dominant effect of span is captured in the  $b^2$  term in the

denominator of Eq. (4). The total span for the unswept configuration can be written as

$$b = b_1 + 2\Delta b \quad (5)$$

where  $b_1$  is the total span of the unextended-span, unswept configuration. Combining Eqs. (3-5), the total drag can be written as

$$D = qS_{ref}C_{dp} \left( 1 + \frac{2\Delta bc}{S_{ref}} \right) + \frac{L^2}{\pi q(b_1 + 2\Delta b)^2} \quad (6)$$

This equation may be used to determine the  $\Delta b$  that achieves a given  $L$  with minimum  $D$ . This is done by taking the derivative of Eq. (6) with respect to  $\Delta b$  and setting it equal to zero. The resulting equation for  $\Delta b$  is as follows

$$\Delta b = \frac{1}{2} \left[ \left( \frac{2L^2}{\pi q^2 C_{dp} c} \right)^{1/3} - b_1 \right] \quad (7)$$

This equation, which is similar to Tucker's result<sup>7</sup>, shows that for minimum drag,  $\Delta b$  varies as  $L^{2/3}$ . Note that  $C_{dp}$  is in the denominator of Eq. (7). This indicates the expected result that as  $C_{dp}$  decreases, meaning the penalty for wetted area decreases, the  $\Delta b$  for minimum drag increases. Figure 10 shows the  $\Delta b$  for minimum drag calculated from Eq. (7) with the geometric constraints for the current aircraft model (defined in Figure 10). This figure shows that, for minimum drag, there is a relatively small range of  $C_L$  values where the span is neither fully extended nor fully retracted. This result will be confirmed from wind tunnel data.

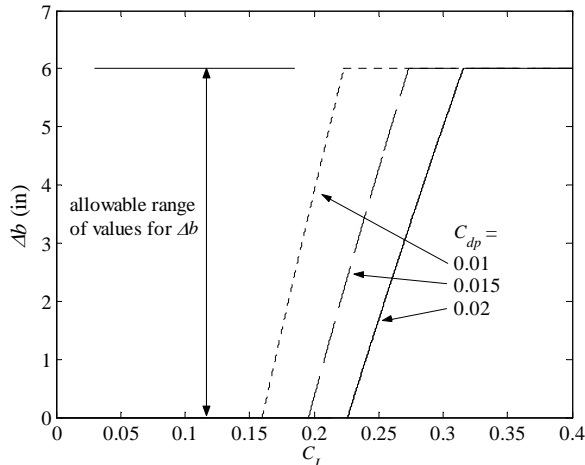


**Figure 11:** Span Extensions ( $\Delta b$ ) for minimum drag calculated from Eq. (7) with the geometric constraints of the current aircraft model

The effect of variable sweep and tail extension on the drag can be approximated by considering the trends seen in the preceding analysis. For instance, assuming

that sweep has little effect on the wing area, the main effect of sweep on Eq. (6) is the change it causes to the projected span (the span projected into the Trefftz plane) and the assumed load distribution. The projected span decreases with sweep, which therefore increases the induced drag. Also, if the load distribution is elliptic when the wing is unswept, the swept load distribution will be less elliptic. These factors indicate that, under the current assumptions, variable sweep is not likely to provide a drag reduction. The same can be said for the tail extension, which only increases the total area with no span increase. Thus, extending the tail increases the profile drag without decreasing the induced drag. It should be mentioned that adding a trim constraint to this discussion would make variable sweep and a tail extension more likely to provide a drag reduction. The wind tunnel data will show beneficial drag properties of sweep at large lift values.

### Wind Tunnel Test Setup

The model was tested in Virginia Tech's 6x6 ft stability wind tunnel. The test condition and reference parameters used to nondimensionalize the force coefficients are shown in Table 1. The reference area ( $S_{ref}$ ) is the planform area of the model with the wings and tail fully retracted and unswept. The length  $x_{ref}$  in Table 1 is the distance from the nose of the model to the reference location for the pitching moment as shown in Figure 12.

**Table 1:** Test condition and reference parameters

$U_{inf}$	73.3 ft/s
$Re_c$	843,000
$S_{ref}$	6.81 ft <sup>2</sup>
$c_{ref}$	1.81 ft
$x_{ref}$	1.37 ft

Figure 12 illustrates the planform variables investigated in this experiment. The span and sweep changes were tested from 0 to 6 inches and 0 to 40 degrees, respectively.

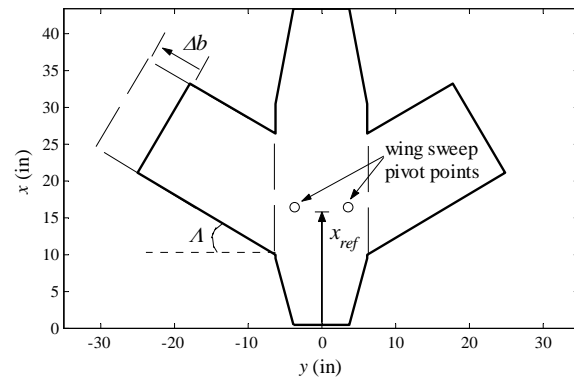


**Figure 12.** Illustration of the planform parameters

The range of the tail extension (not shown in Figure 12) is from 0 to 6 inches. Wind tunnel data will be presented for the unextended tail case only. Figure 13 shows the vehicle mounted in the Stability Tunnel for testing.



Figure 13. Experimental model mounted in Stability Tunnel

### Wind Tunnel Test Results

The goal of the wind tunnel test was to determine the influence of the planform variables (sweep, span extension, and tail extension) on the model's aerodynamic characteristics. Of particular interest was the effect of the planform variables on the aerodynamic center location and the drag force.

Figure 14 shows the shift in the aerodynamic center location ( $x_{ac}$ ) with sweep for different values of span extension. It is expected that as the sweep increases, the aerodynamic center should shift aft. This result is seen in Figure 14. In addition, as the span being swept increases, the shift in aerodynamic center increases. The aerodynamic center shifts 19.5% of  $c_{ref}$  for  $\Delta b = 0$ , 22.3% for  $\Delta b = 50\%$ , and 25.7% for  $\Delta b = 100\%$ . The influence of these aerodynamic center shifts on the aircraft stability depends on the location of the aircraft's  $c.g.$ . Thus, knowledge of the shift in the  $c.g.$  with a planform variation is necessary to assess the influence of the planform variation on the aircraft stability. From Eq. (1), it is found that the  $c.g.$  shifts 11% of  $c_{ref}$  as the aircraft changes from the unextended, unswept to the fully extended fully swept configuration. This reduces the shift in the static margin. Figure 14 indicates that  $C_{M\alpha}$  becomes more stable (more negative) as sweep increases. In an extreme case, if the  $c.g.$  shift was larger than the aerodynamic center shift,  $C_{M\alpha}$  would become more unstable (more positive) as the sweep increased.

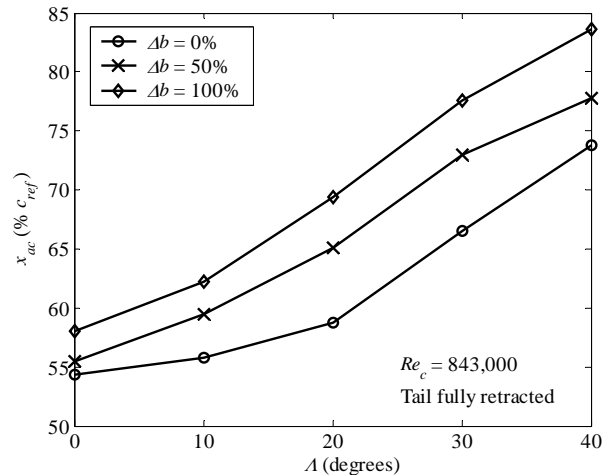


Figure 14. The influence of span extension ( $\Delta b$ ) and sweep ( $\Lambda$ ) on the aerodynamic center location.

The variation of  $C_{L\alpha}$  with sweep for different values of span extension is shown in Figure 15. The same reference area ( $S_{ref}$ ), shown in Table 1, is used for the  $C_{L\alpha}$  calculation of every configuration. It is seen in Figure 15 that  $C_{L\alpha}$  decreases with increasing sweep. For  $\Delta b = 0$ ,  $C_{L\alpha}$  changes by 14.2% as  $\Lambda$  changes from 0 and 40 degrees. The percent change for the  $\Delta b = 50\%$  and  $\Delta b = 100\%$  cases are 15.9% and 14.6%, respectively. This indicates that, as expected, the change in  $C_{L\alpha}$  is less sensitive than the aerodynamic center to sweep changes.

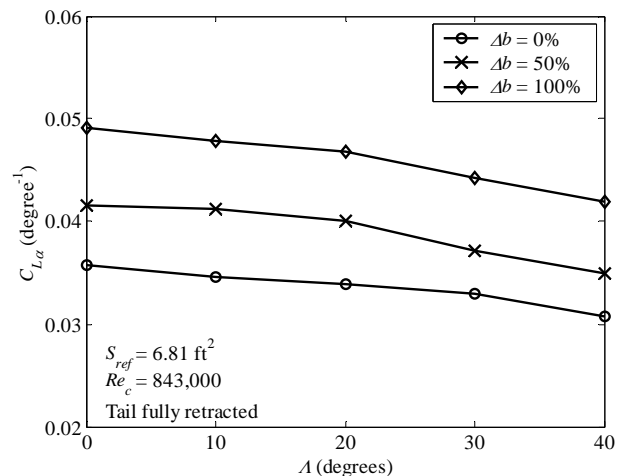


Figure 15. The influence of span extension ( $\Delta b$ ) and sweep ( $\Lambda$ ) on the lift curve slope ( $C_{L\alpha}$ ).

It was shown in Figures 14 and 15 that variable planform capability allows for significant changes in the stability of the aircraft. The following will examine the influence of planform variations on the drag. Figures 16 and 17 show the drag polars for the unswept

and fully swept configurations. These plots illustrate the basic concept of Eqs. (6) and (7), which indicate that at low  $C_L$  values, where the induced drag is small, the profile drag is dominant. Because the profile drag is proportional to the wing area (Eq. 3), and the wing area is proportional to the span (Eq. 2), Figures 16 and 17 show that the  $\Delta b = 0$  cases have the minimum drag at low  $C_L$  values. On the other hand, for high  $C_L$  values, the induced drag dominates as indicated by Eq. (4). The induced drag is inversely proportional to the span squared. Thus, Figures 16 and 17 show that the  $\Delta b = 100\%$  cases have the minimum drag at high  $C_L$  values. Notice that the three  $\Delta b$  cases intersect at nearly the same  $C_L$  value. This confirms the observation made previously in Figure 11 that there is only a small range of  $C_L$  values where the minimum drag is obtained with a span that is neither the minimum nor maximum.

An interesting aspect of Figures 16 and 17 is that, although the model is entirely uncambered, the minimum drag does not occur at  $C_L = 0$ . This is likely due to inadvertent twist in the outboard wing section.

The influence of sweep on the lift and drag can be examined from Figures 16 and 17. The two major effects appear to be an increase in both the minimum  $C_D$  and the maximum  $C_L$  ( $C_{Lmax}$ ) for the fully swept case. The increase in the minimum  $C_D$  for the fully swept case is likely caused by the wing tips acting as a trailing edge as the sweep increases. The edges of the wing tips were flat, and therefore created an additional base drag component. At 40-degree sweep with the full span wing, the tip represents 30% of the aircraft's trailing edge.

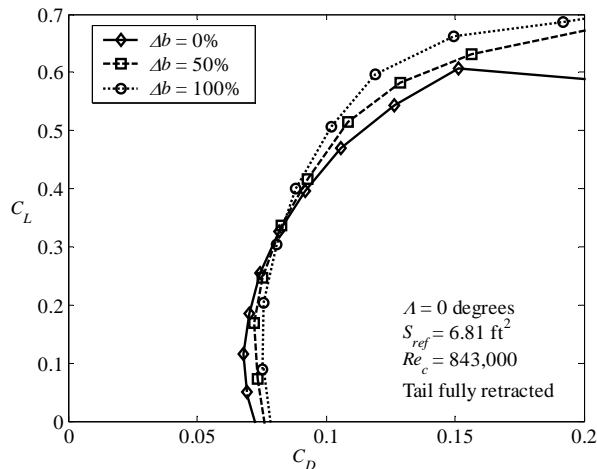


Figure 16. The influence of span extension on the drag for the unswept case

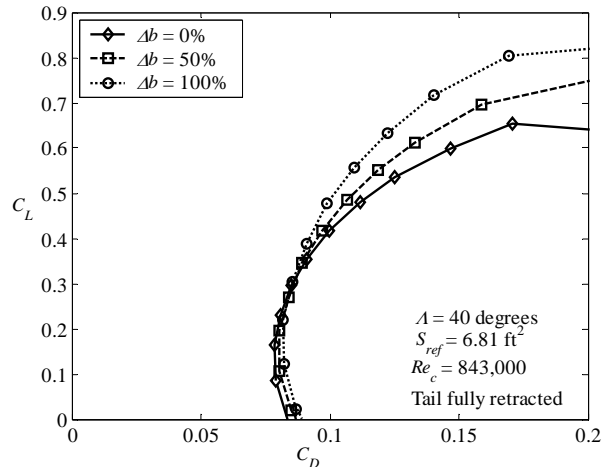


Figure 17. The influence of span extension on the drag for the fully swept case

An unexpected result shown in Figure 16 and 17 is the increase in  $C_{Lmax}$  for the fully swept case over that of the unswept case. For further insight into this observation,  $C_L$  and  $C_M$  are plotted vs. angle of attack in Figures 18 and 19 for the unswept and fully swept case. These plots show that although the nonlinear “break” in the  $C_M$  curve occurs at the same angle of attack for both cases, the  $C_L$  for the unswept case breaks much earlier than for the swept case. This indicates that although flow separation begins at the same angle of attack for both cases, the swept case is able to obtain more lift on the inboard section of the wing and on the fuselage. This explains the sharp  $C_M$  break but continued linear  $C_L$  increase shown in Figures 18 and 19 for the swept case.

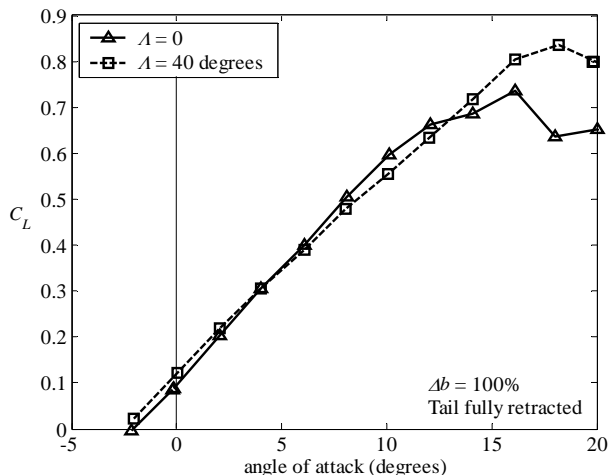
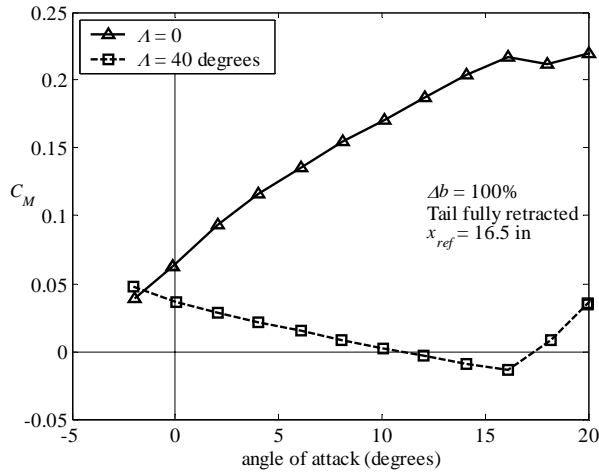
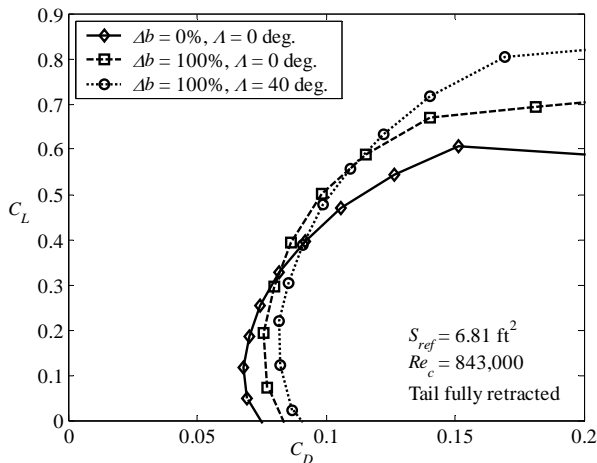


Figure 18. Lift coefficient vs. angle of attack for an unswept and fully swept configuration



**Figure 19.** Pitching moment coefficient vs. angle of attack for an unswept and fully swept configuration

The variable planform optimum drag polar is shown in Figure 20. This shows that three planform geometries are required to maintain minimum drag over the range of possible  $C_L$  values. This idea was discussed in the previous section and shown in Figure 11 and Eq. (7). The presence of the unswept  $\Delta b = 0$  and 100% cases in Figure 20 are predicted from Eq. (7). The presence of the swept case for minimum drag at large  $C_L$  values is a result of the previously discussed high-lift capability of the fully swept case.



**Figure 20.** The reduction of drag over a range of lift coefficients through planform variations

### Conclusions

The adaptive aircraft testbed, designed and constructed for large configuration changes, is capable of five independent planform variations along with independent twist control for each wing. The vehicle undergoes a 38% increase in span, 40 degrees of sweep change, 12% change in chord length and  $\pm 20$  degrees of wing twist. The *c.g.* location shifts from 31.46% to

42.47% of the reference chord from zero sweep to full extension and sweep.

Wind tunnel results showed that variable planform capability allows low drag to be maintained throughout a range of lift coefficients. An approximate analysis quantified the planform changes required to maintain minimum drag. The ability to change both sweep and span was shown to be beneficial.

### Acknowledgements

The authors would like to thank the National Science Foundation and the Virginia Space Grant Consortium for funding.

### References

- 1) Bowman, J., Sanders, B., Weisshaar, T., "Evaluating the Impact of Morphing Technologies on Aircraft Performance," AIAA paper 2002-1631, 2002.
- 2) Roth, B., Peters, C., Crossley, W., "Aircraft Sizing with Morphing as an Independent Variable, Strategies and Investigation," AIAA paper 2002-5840, 2002.
- 3) Martin, E. T., Crossley, W., "Multiobjective Aircraft Design to Investigate Potential Geometric Morphing Features," AIAA paper 2002-5859, 2002.
- 4) Marmier, P., Wereley, N., "Morphing Wings of a Small Scale UAV Using Inflatable Actuators for Sweep Control," AIAA paper 2003-7837, 2003.
- 5) Blondeau, J., Richeson, J., Pines, D., "Design of a Morphing Aspect Ratio Wing Using an Inflatable Telescoping Spar," AIAA paper 2003-1718, 2003
- 6) Tucker, V. A., "Gliding Birds: The Effect of Variable Wing Span," *Journal of Experimental Biology*, Vol. 133, 1987, pp. 33-58.
- 7) Tucker, V. A., Parrott, G. C., "Aerodynamics of Gliding Flight in a Falcon and other Birds," *Journal of Experimental Biology*, Vol. 52, 1970, pp. 345-367.
- 8) Kress, R. W., "Variable Sweep Wing Design," AIAA 80-3043, 1980.
- 9) Poisson-Quinton, P., "Aerodynamics of Variable Sweep," AGARD Assessment of Lift Augmentation Devices, LS-43, 1971.

